CHAPTER IV

RESULTS AND DISCUSSION

The characteristics of flow in constricted parallel ducts with the 14:1 aspect ratio rectangular duct were carried out using an experimental investigation for various flow levels in the laminar range up to the transition Reynolds number. Three ratio of free-flow area to frontal area of the constriction, σ's, (which are 1/4, 1/2 and 2/3) were selected. The ratio of the constriction length to hydraulic diameter, L/D_h was also varied from 2 to 100. Reynolds number can be gradually increased by changing the rate of flow. The experiment on the constricted parallel ducts for various σ and L/D_h was successively carried out with an increment of pressure difference. Results are presented graphically in Fig.4.9 to Fig.4.17, covering laminar and transition flow regimes. The corresponding tabulated results and sample of calculation are also presented in Appendix A.

4.1 Long Constriction

The presentation and discussion of results for long constriction will be subdivided into two parts. The first section is devoted to the static pressure distribution and pressure drop, while the second section is concerned with the loss coefficients and friction factor.

Pressure Distributions and Pressure Drops

A major focus of the fluid flow experiments was to determine the net pressure drops, ΔP_c, ΔP_e and ΔP_f, due to abrupt contraction, abrupt expansion and skin friction in constriction duct respectively. This information was deduced from working graphs in which the static pressure distribution along the hydrodynamic development length and the test section including exit section was plotted for each of the data runs. The maximum value of L/D_h (which is 100) was herein considered to be long constriction duct. typical working graph is presented in Fig.4.11 (the graph is for σ = 1/4, L/D_h = 100 and Re = 1420). In this figure, the static

pressure, P^* is plotted the ordinated, where P^* is the pressure at axial station x. Note that for the fluid flow studies, the axial co-ordinate, denoted by x, is equidistant with the constriction length, L when it is measured from the upstream face of the constriction that the flow separation is initiated, avoiding the negative value. The x coordinate is illustrated in Fig.4.8. It is seen from Fig.4.11 that the pressure distribution upstream and along of the constriction is linear, indicating hydrodynamically developed flow. Furthermore, downstream of the constriction, after a region of readjustment, fully developed conditions are restored as witnessed by linearity of the pressure distribution. Straight lines were respectively passed through the upstream, constriction and downstream linear pressure data: As illustrated in Fig. 4.11, each line was extrapolated to x = 1 and 2 to give the pressure that would have existed at that station had fully developed laminar duct flow existed in the respective parallel ducts (i.e., in the absence of the constriction). The upstream, constriction and downstream extrapolations yield different pressure, as can be seen in Fig. 4.11. The differences between the upstream and constriction and between the constriction and downstream are the net pressure loss ΔP_c and ΔP_e, respectively, due to the presence of the constriction. While the pressure loss, ΔP_f is due to a flow friction in the constriction. It is the net result of all pressure-related processes, including acceleration and deceleration, separation and reattachment, dissipation in the recirculating region, and post-reattachment redevelopment of flow.

Since ΔP is primarily an inertial loss, it is natural to refer it to the velocity head $(\rho V^2)/2$ in order to obtain a dimensionless results. Due to V^2 can be changed to b^2/ν^2 form, the static pressure distribution along mid-channel will now be presented in terms of the dimensionless variable defined as $P^* g_c b^2/\rho\nu^2$. Since P^* and $(b^2/\rho\nu^2)$ are constants for a given data run, the axial distribution of this variable is a true reflection of the behavior of the pressure itself. The pressure results to be presented are for Re about 1500 and various σ and L/D_h. The dimensionless pressure distribution for $\sigma = 1/4$ and $L/D_h = 100$, is already available in Fig. 4.11 when reference is made to the

right-hand ordinate; the distribution curves for σ = 1/2 and 2/3 are respectively presented in Fig. 4.12 and 4.13. It is seen from these figure that the effect of pressure change, at the constriction entrance and exit, took place only at a very short distance compared with the constriction length. The experimental results obtained here agree quite well with analytical result,[3], Fig. 4.13a.

Loss Coefficients and Friction Factor

The contraction coefficient, K_c, the expansion coefficient, K_e and Fanning friction factor, f which express the net pressure loss due to the presence of the constriction were evaluated in accordance with the following equation;

$$K_c = \Delta P_c^* . 2g_c/\rho V^2 - 1 + \sigma^2 \qquad \text{.....(4.1)}$$

$$K_e = \Delta P_e^* . 2g_c/\rho V^2 + 1 - \sigma^2 \qquad \text{.....(4.2)}$$

$$f = \Delta P_f/4(L/D_h)\,\rho\,(V^2/2g_c) \qquad \text{.....(4.3)}$$

where, ΔP_c^* = net pressure drop due to sudden contraction,
ΔP_e^* = net pressure drop due to sudden expansion,
ΔP_f = net pressure drop due to flow friction inside the constriction,
V = mean velocity in the constriction duct,
ρ = density of working fluid,
g_c = conversion factor

ΔP_c^*, ΔP_e^* and ΔP_f for each area ratio are presented in table A to C and loss coefficients and friction factor are also list in table A to C in Appendix A. The table contains results for three area ratio, σ (1/4, 1/2 and 2/3), L/D_h = 100 and for Reynolds number ranging from 200 to 4000. The results thus obtained are also plotted in Fig. 4.10. The figure shows the variation of K_c and K_e with the area ratio, σ, for various Reynolds number up to 2000, i.e., Re = 200, 500, 1000, 1500 and 2000. The results for higher Re obtained through extrapolation are also included in transition regime. The numerical results, [1,3], for K_c and K_e are shown in Fig. 4.10a for comparison. The agreement of both curves is remarkably good. The Fanning friction factor, f, found to be about 24/Re, agree with those results published.

The "critical" constriction length, L_c, is obtained from the Fig. 4.14 and is found to be,

$$L_c/D_h = C\ Re \cdot \sigma^{3/4} \qquad \text{.....(4.4)}$$

where L_c is defined as the minimum constriction length beyond which the loss coefficients remain constant, and the range of C is from 0.7 to 1.0, all within the range normally analyzed from the trend of the data in Fig. 4.14. The average of C is 0.87.

In computing the physical properties of water which are density and kinematic viscosity, based on the bulk temperature of water, were obtained from ASCE Manual Eng. Pract., Hydraulic Models in reference [22].

4.2 Short Constriction

The presentation and discussion of results for short constriction will be also subdivided into two parts.

Loss Coefficients and Friction Factor

Experimental results for short constrictions were obtained for the loss coefficients, K_c^* and K_e^*, Fanning friction factor, f^*. In computation these values are the same long constriction case. The values of loss coefficients and Fanning friction factor are given in the form of correction factors between the values of long and short ducts as well as [2,3], i.e., correction factor for contraction coefficient, C_c, for expansion coefficient, C_e and for Fanning friction factor, C_f, which are defined as follows:

$$\left.\begin{aligned} K_c^* &= C_c . K_c \\ K_e^* &= C_e . K_e \\ f^* &= C_f . f \end{aligned}\right\} \qquad \text{.....(4.5)}$$

Here, K_c and K_e are the loss coefficients and f denotes the Fanning friction factor for flow through parallel ducts with a long constriction. Both K_c and K_e are determined from Fig. 4.10. f corresponds to that for flows through parallel ducts with aspect ratio 14:1 and is equal to 22/Re by evaluating from Fig. 4.9. The correction factor C_c, C_e and C_f, derived from the computations, are plotted against B_F in Fig.4.14, where B_F defined as $(Re.D_h/L)^{1/3}$ $\sigma^{1/4}$. From inspection of the Fig.4.14, reveals that they are unity

when $B_F \leq 2.25$, approximately, the criterion for a constriction to be hydrodynamically long. Short constriction satisfies the condition of $B_F > 2.25$. The correction factor in Fig.4.14, inwhich a dashed line has been faired through the data points, can be expressed in the form of

$$C = aB_F + b \qquad \text{.....(4.6)}$$

in which a = -0.25, 2/3, 0.125 and b = 1.5, -0.5, 0.73 for C_c, C_e and C_f, respectively. The correction factor results from Bunditkul's analysis are represented by solid line in Fig. 4.14, and obtain a = -0.304, 0.792, 0.122 and b = 1.684, -0.782, 0.725 for C_c, C_e and C_f, respectively. Turning first to the comparison of analysis and experiment in Fig.4.14, they agree quite well for $B_F \leq 2.25$, the deviations are about 20 to 40% for $B_F > 2.25$. The discrepancy is partly due to the effect of the variation of fluid properties with temperature. Furthermore, the deviations may probably be caused by systematic errors occuring during calibration of equipments, and random errors being the fluctuations in observations which yield results that differed from experiment to experiment. The deviation may also be due to an effect of duct corners at the upstream face of the constriction which were not really sharp as assumed in the theory because of the method of construction. Moreover, it is important to observe that an error should be due to the effect of the duct sides since Bunditkul did not treat the duct of 14:1 aspect ratio but providing numerical results for the duct of infinite aspect ratio. Hence the disparity is somewhat large in the case of small value of L/D_h.

In order to ascertain whether there is possible effect of transition flow on the discrepancies, Fig. 4.14a has been replotted for correction factors, C_c, C_e and C_f against B_F with Re < 1600. It is readily seen that the experimental results obtained fit in perfectly with those found from numerical analysis [2,3]. Thus it may be concluded that, beyond Re 1600, experiments performed were in the transitional range and the flow was not a perfect laminar. As a consequence, a deviation of experimental data from numerical prediction took place, as already shown in earlier Fig. 4.14.

Pressure Distributions and Pressure Drops

Measurements of axial pressure distribution for short constriction are the same long constriction case and are presented in Fig.4.15 to 4.17 for small L/D_h by corresponding B_F as aforementioned. All of the pressure distribution have similar shapes. The pressure drops slowly in the fully developed duct flow upstream of the constriction and then precipitously due to acceleration of the fluid when passing through a constriction. This is followed by a pressure recovery as the mainflow progressively fill more and more of the duct cross section. The recovery ceases when the mainflow fills the entire cross section, and there the pressure begins to drop as the flow redevelops and continues to drop as friction takes its toll in the fully developed regime.

The pressure drops ΔP_c^* and ΔP_e^*, due to an abrupt contraction and expansion, determining the loss coefficient, K_c^* and K_e^* for flow in parallel duct with short constriction using the same equation for long constriction case. And Fanning friction factor, f^* is also determined. The hydrodynamic entrance effect is exhibited as a pressure variation immediately downstream from the inlet, $x/L = 1$ to about 1.2, while the hydrodynamic exit effect appear as the pressure change immediately upstream from the exit, $x/L = 1.6$ to 2. These effects agree with the analysis of Bunditkul [2,3]. The onset of the linear pressure variation, signalling redevelopment of flow, occurs at about 3D from downstream face of the constriction. This redevelopment appears to be remarkably rapid, especially in view of the severe disturbances that are inflicted on the flow by the smaller area ratio. As the constriction grows in length, the pressure variations at the entrance and exit reduce in magnitude.

4.3 Qualitative Comparison

Visualization of flow in parallel ducts with abrupt contraction and expansion is shown in Fig.4.1 through 4.6, for $L/D_h = 5$, $\sigma = 1/4$ and various Re. The pictures were visualized by continuous dye injection through the ducts. The dividing streamline is clearly seen along the constriction with the separation point and recirculating flow regions. Considering all

pictures, there are three recirculating flow regions; the first at the concave corner, the second on the constricted or step surface and the third behind the constriction or steps. The three regions are separated by a dividing streamline. Fig.4.1 shows the streamline passing through the constriction and parallel the duct, Figs. 4.2, 4.3 and 4.4 present a dividing streamline, smooth curves of streamline and profile of streamline before entering the constriction, respectively while Figs. 4.5 and 4.6 reveal the recirculating flow regions at back corner and on the step or constricted surface (called "vena contracta"), respectively, with a dividing streamline. Numerical results by Bunditkul [2,3] for flow in a duct with sudden contraction and expansion at $Re = 600$, $L/D_h = 1.0$, $\sigma = 0.5$ is illustrated for qualitative comparison, as shown in Fig. 4.7. This picture is generated by computer graphic and by a method of interpolation and smooth curve fitting. The picture displays the recirculating flow regions at front-and back-corners and on the constricted surface with a dividing streamline. Inspection of these pictures, reveals good qualitative agreement with comparison between analytical results for flow and those pictures obtained by flow visualization.

4.4 Quantitative Comparison

The experimental investigation was employed to examine loss coefficients and friction factor in parallel ducts with abrupt contraction and expansion. The loss coefficients (K_c and K_e) and the three area ratio (1/4, 1/2 and 2/3), for Reynolds numbers ranging from 200 to 4000, are presented in Fig. 4.10, while Fig. 4.14 is illustrated the values of correction factor which are plotted against B_F in case of a short constriction. Further comparisons between experimental and analytical results of loss coefficients for long constriction are shown in Fig.4.10 and Fig. 4.10a. Inspection of these figure reveals that the trends of curves are somewhat similar except for the values of K_e, which are lower and K_c, which are higher, than analytical results, [1,3]. From the correction factor figure, Fig. 4.14, it is seen that very good quantitative agreement is evident at small value of B_F or long constricted duct case. Data points of C_c, C_e and C_f

indicate a tendency toward intersection at about $B_F = 2.25$, although the values of these correction factor differ from that obtained by the numerical analysis of Bunditkul[2,3] when $B_F > 2.25$, or short constricted duct case.

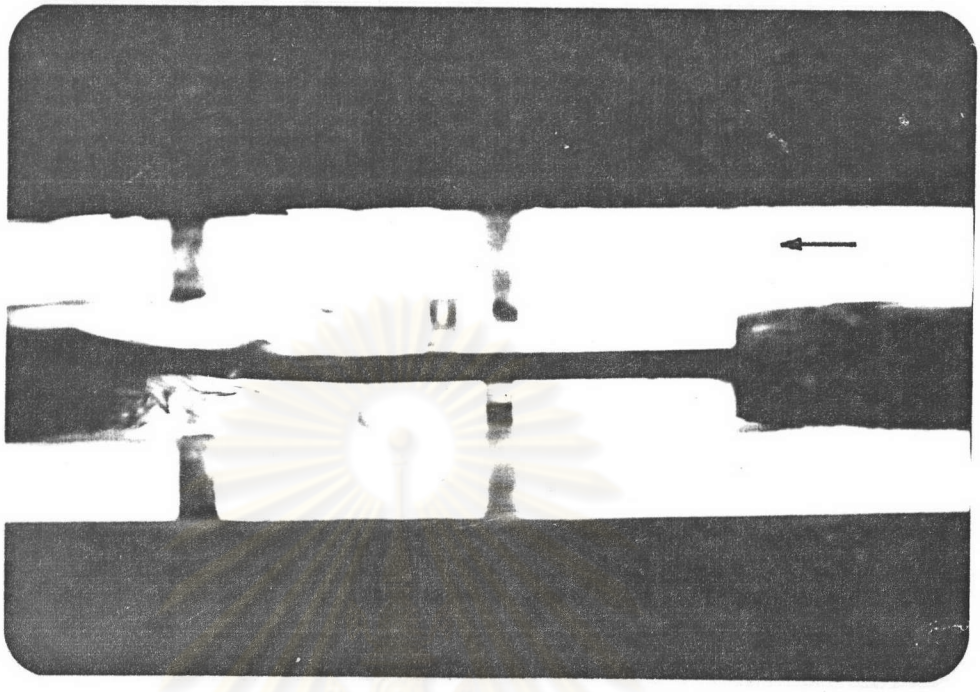

Fig. 4.1 Flow through the constriction for $\sigma = 1/4$, $L/D_h = 5$, and Re = 1500.

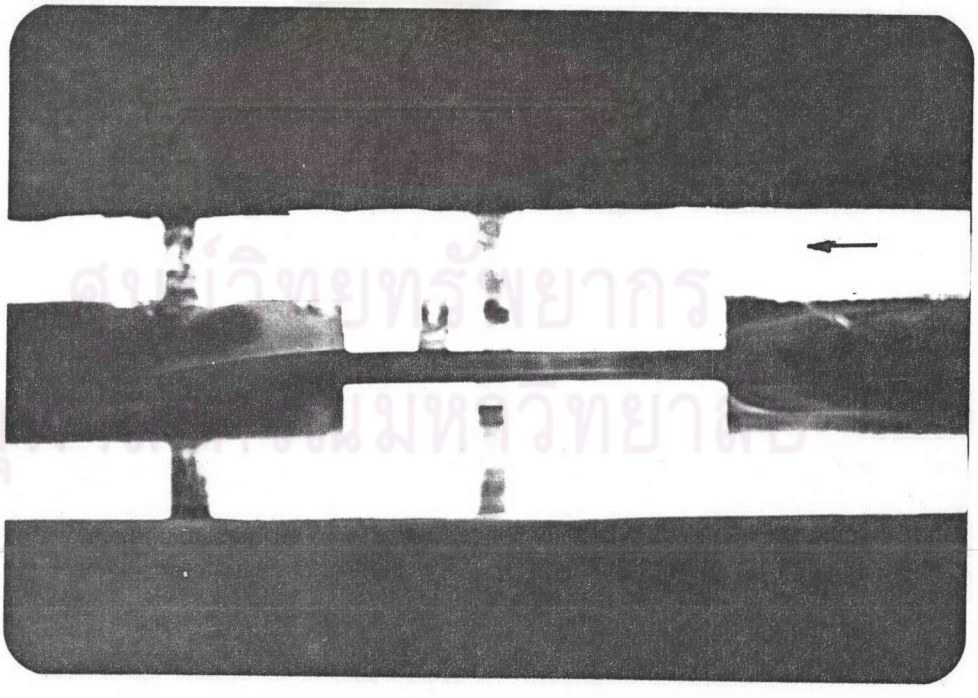

Fig. 4.2 Dividing curves of streamline before passing through the constriction for $\sigma = 1/4$, $L/D_h = 5$, Re = 1500.

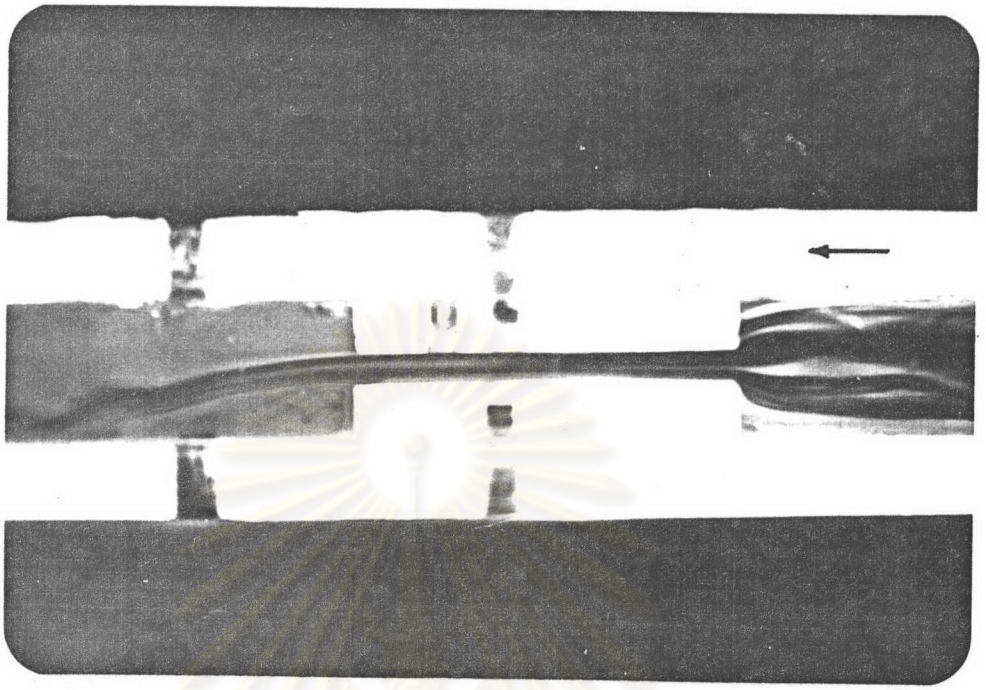

Fig. 4.3 Smooth curves of streamline through the constriction for $\sigma = 1/4$, $L/D_h = 5$ and $Re = 1500$.

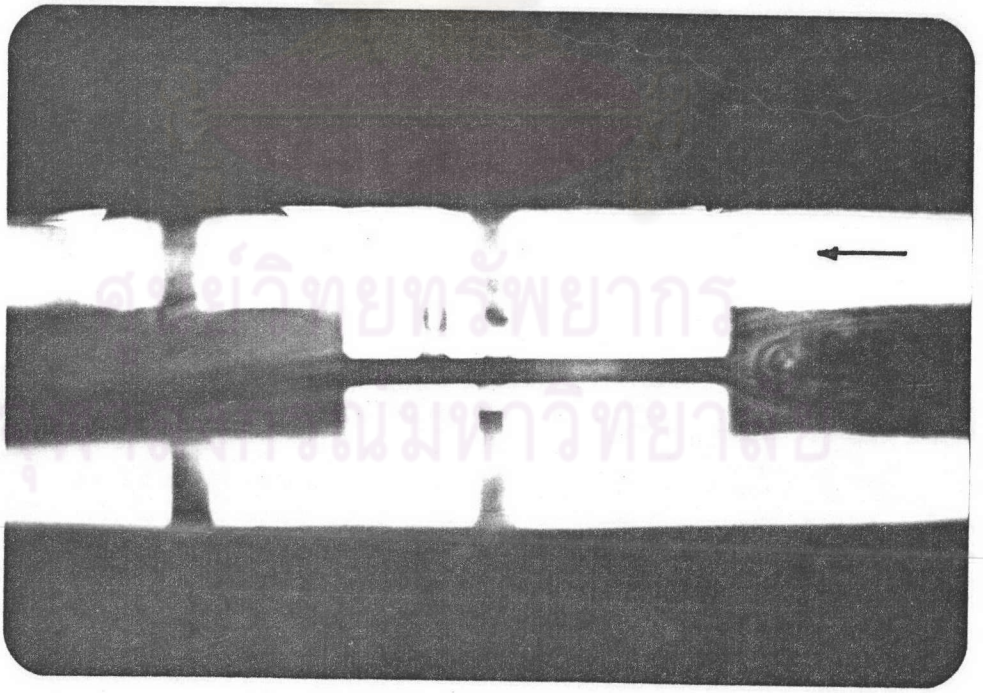

Fig. 4.4 Profile of streamline before facing the constriction for $\sigma = 1/4$, $L/D_h = 5$ and $Re = 1500$.

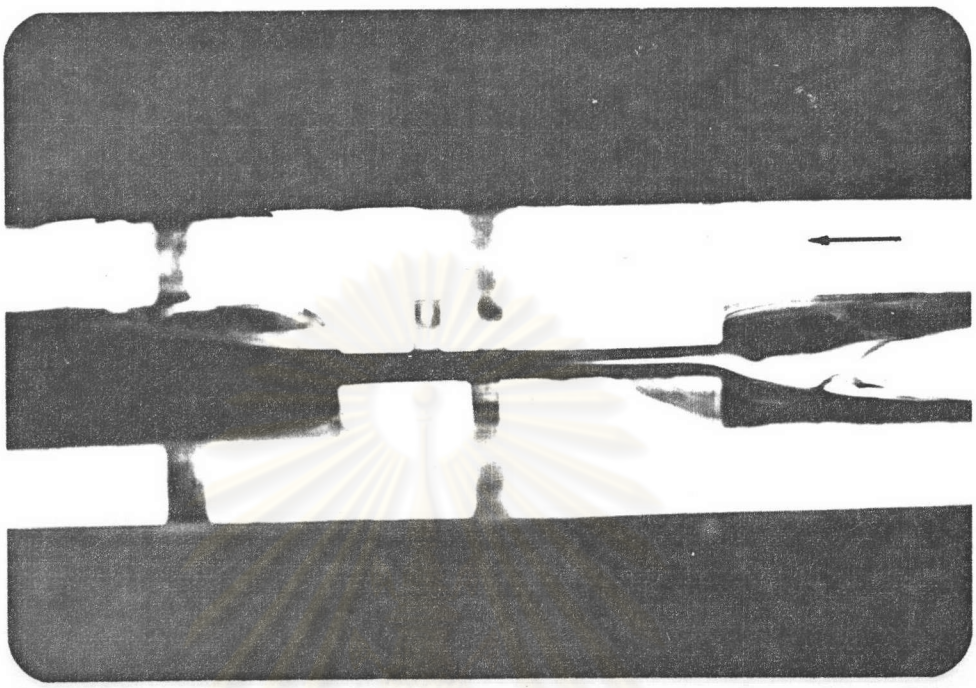

Fig. 4.5 Recirculating region at back-corner for $\sigma = 1/4$, $L/D_h = 5$ and $Re = 1500$.

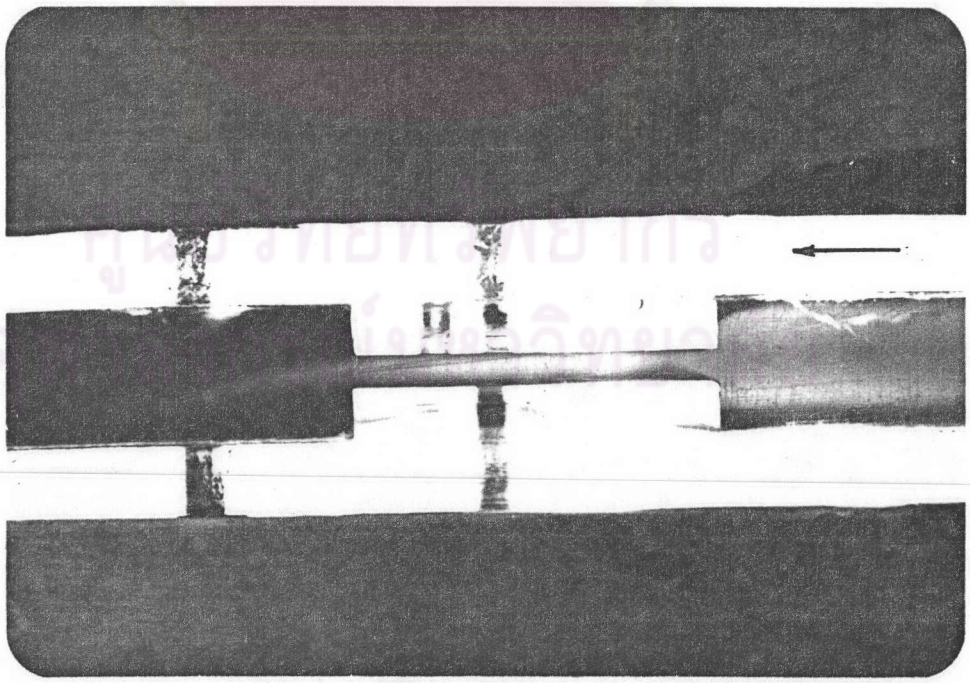

Fig. 4.6 Recirculating region on the constricted surface for $\sigma = 1/4$, $L/D_h = 5$ and $Re = 1000$.

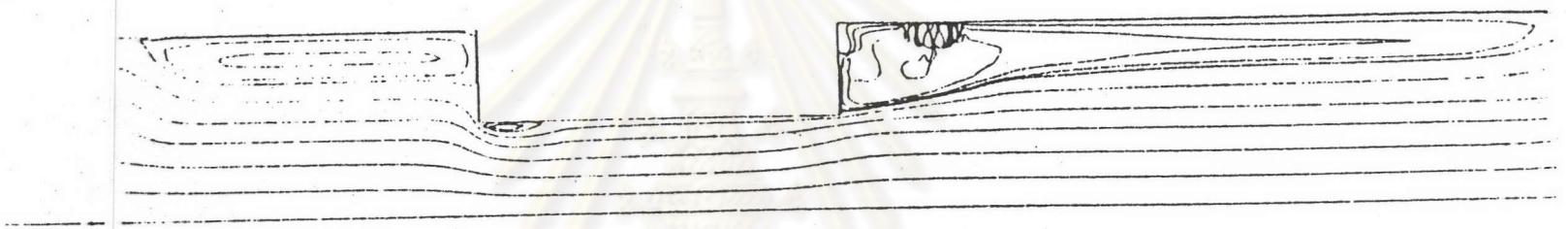

RE_{CORE} = 600.0

L_{CORE}/DH_{CORE} = 1.00000

$A_{CORE}/A_{ENTRANCE}$ = 0.50000

Fig.4.7 Streamlines for Re = 600, L/D_h = 1.0, α = 0.5. by numerical analysis [3]

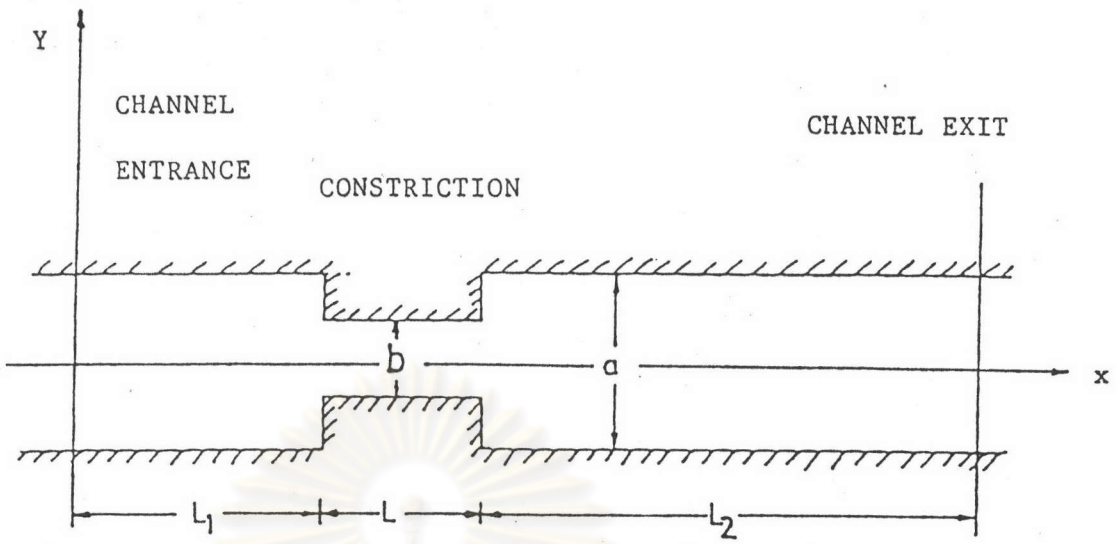

Fig. 4.8 Diagram of a constricted duct configuration and coordinate system.

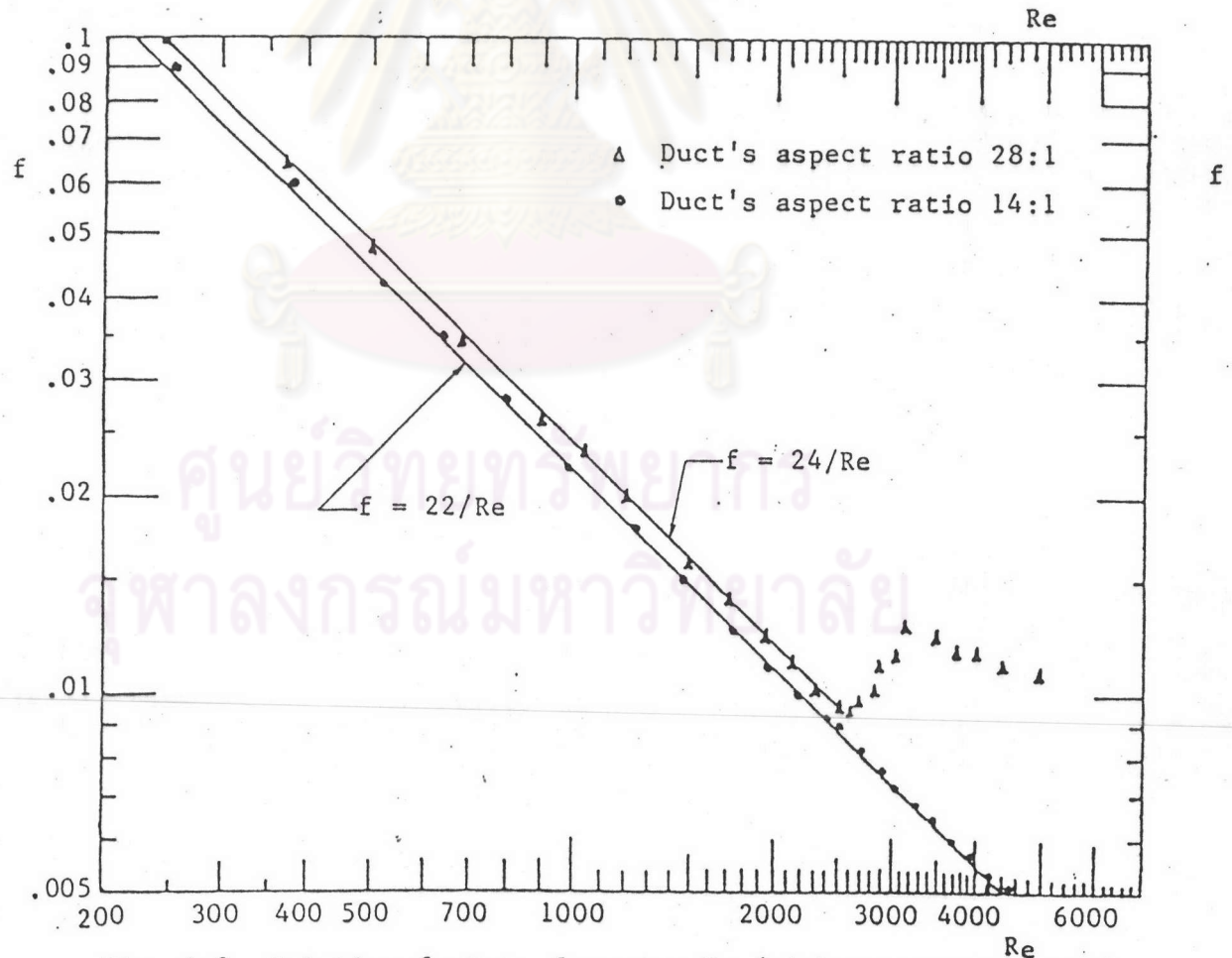

Fig. 4.9 Friction factor, f versus Re (without constriction).

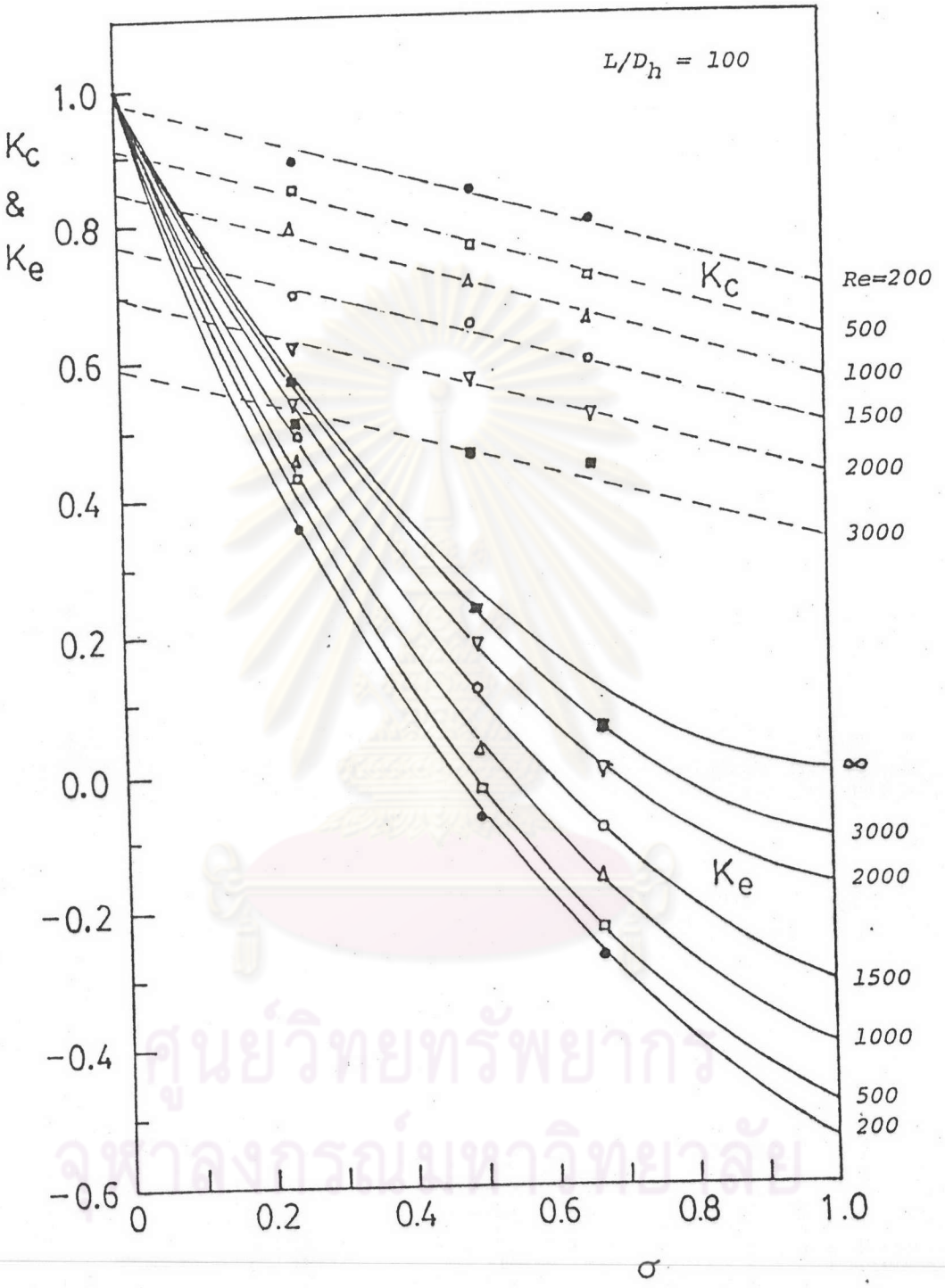

Fig. 4.10 Loss coefficients K_c and K_e versus area ratio σ

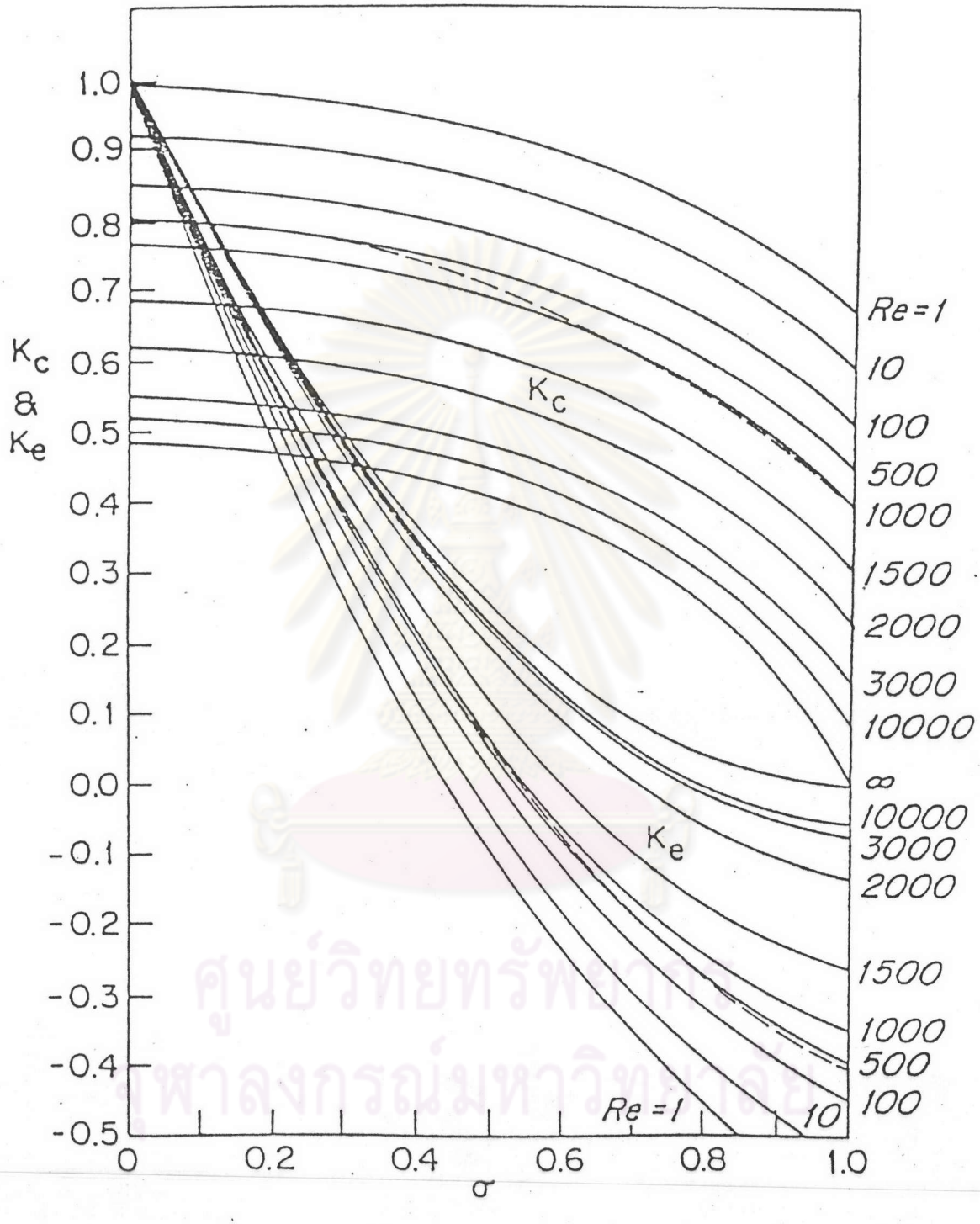

Fig.4.10a Loss coefficients K_c and K_e versus area ratio σ (---- Kays' semi-empirical result for laminar flows). [3]

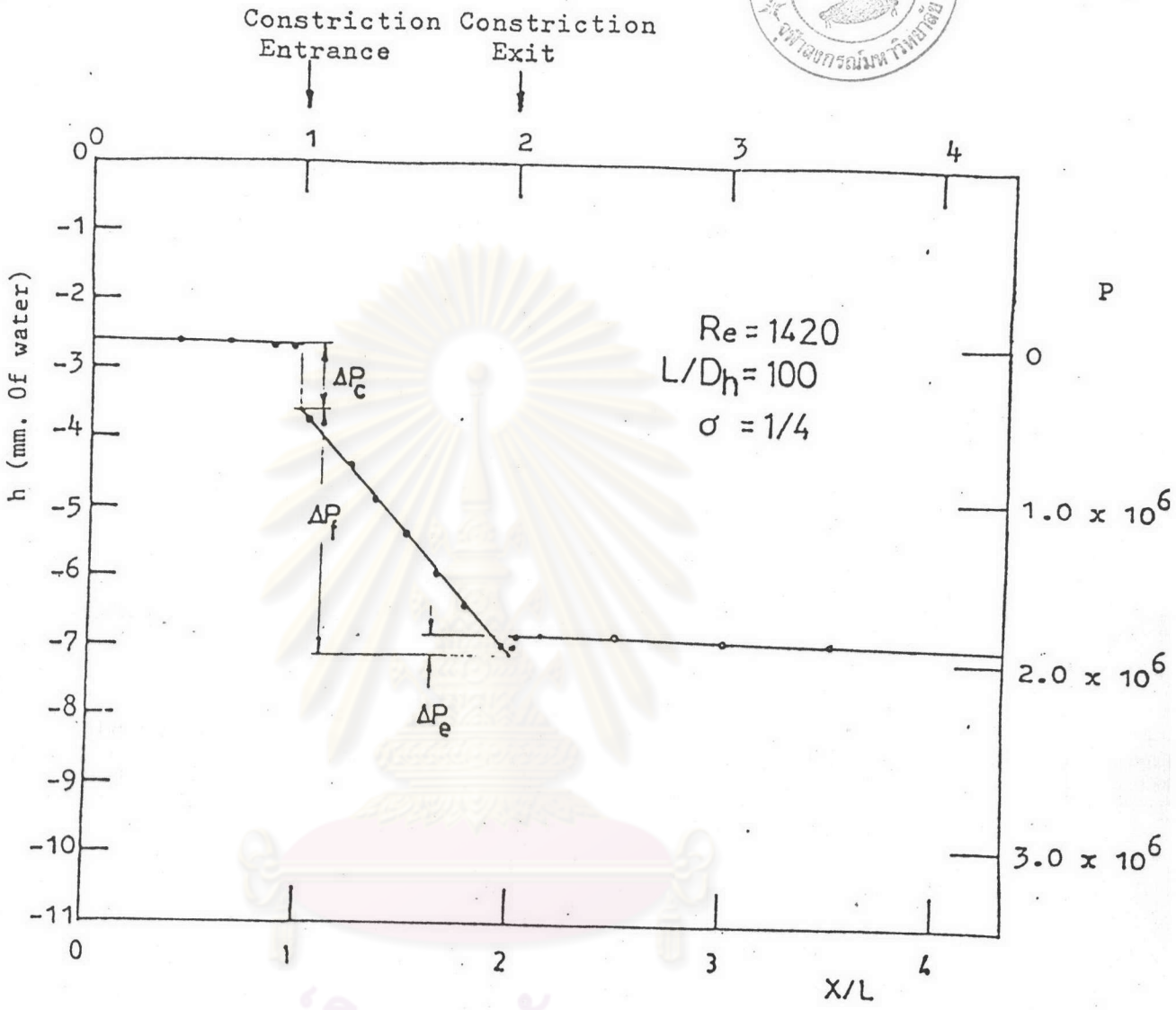

Fig. 4.11 Representative working graph illustrating determination of pressure loss due to the constriction duct; $\sigma = 1/4$, $L/D_h = 100$, Re = 1420. The right-hand ordinate give the dimensionless pressure distribution.

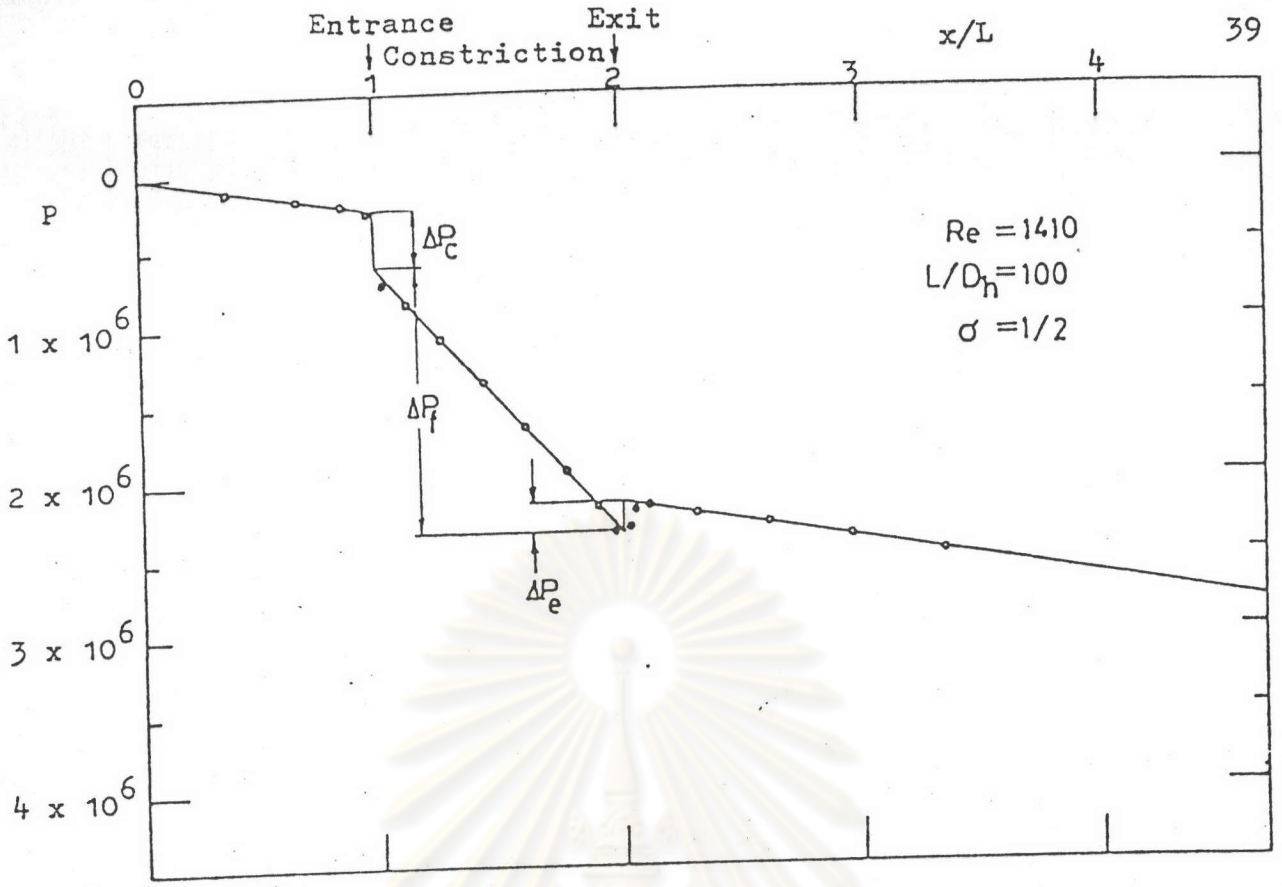

Fig. 4.12 Dimensionless axial pressure distribution for $\sigma = 1/2$, $L/D_h = 100$ and $Re = 1410$.

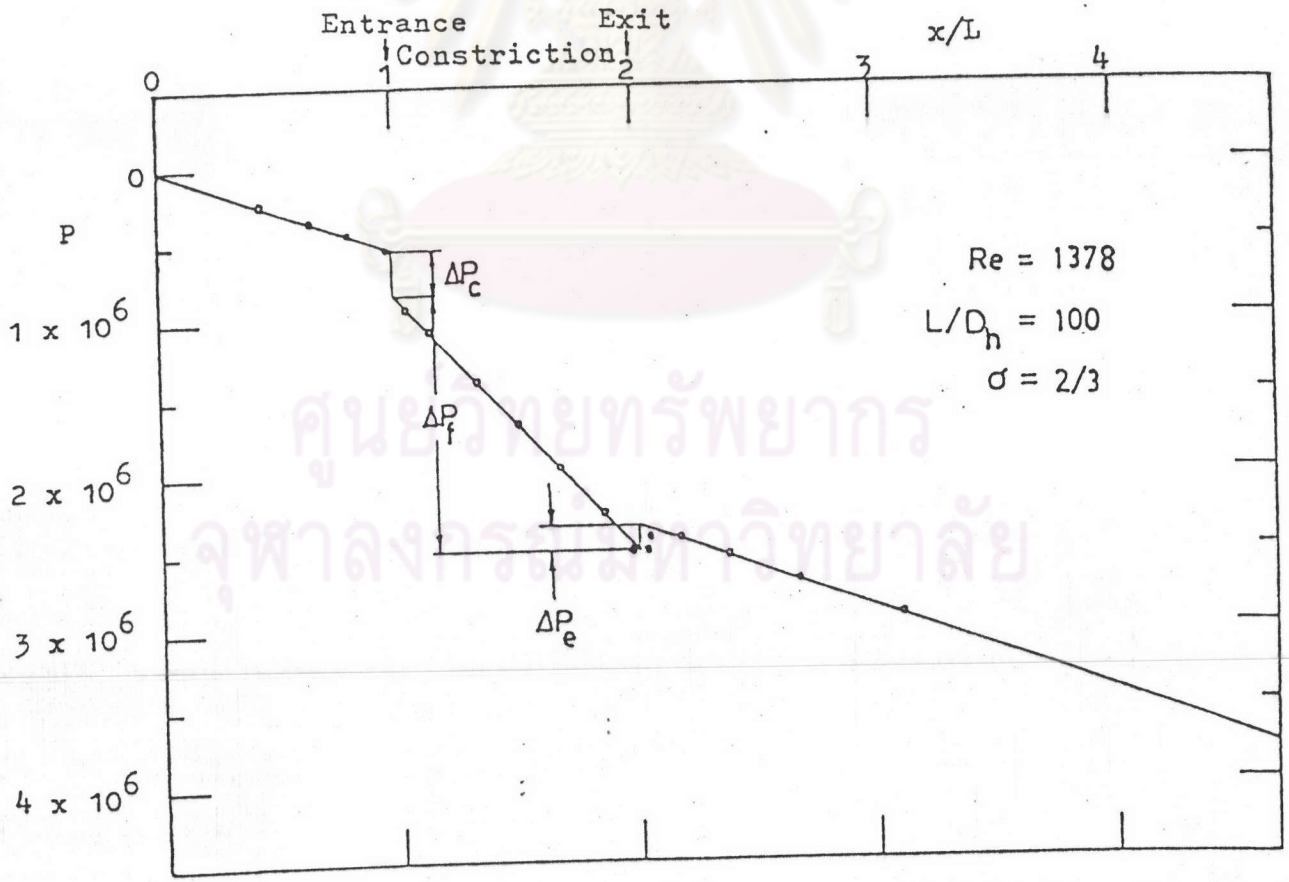

Fig. 4.13 Dimensionless axial pressure distribution for $\sigma = 2/3$, $L/D_h = 100$ and $Re = 1378$.

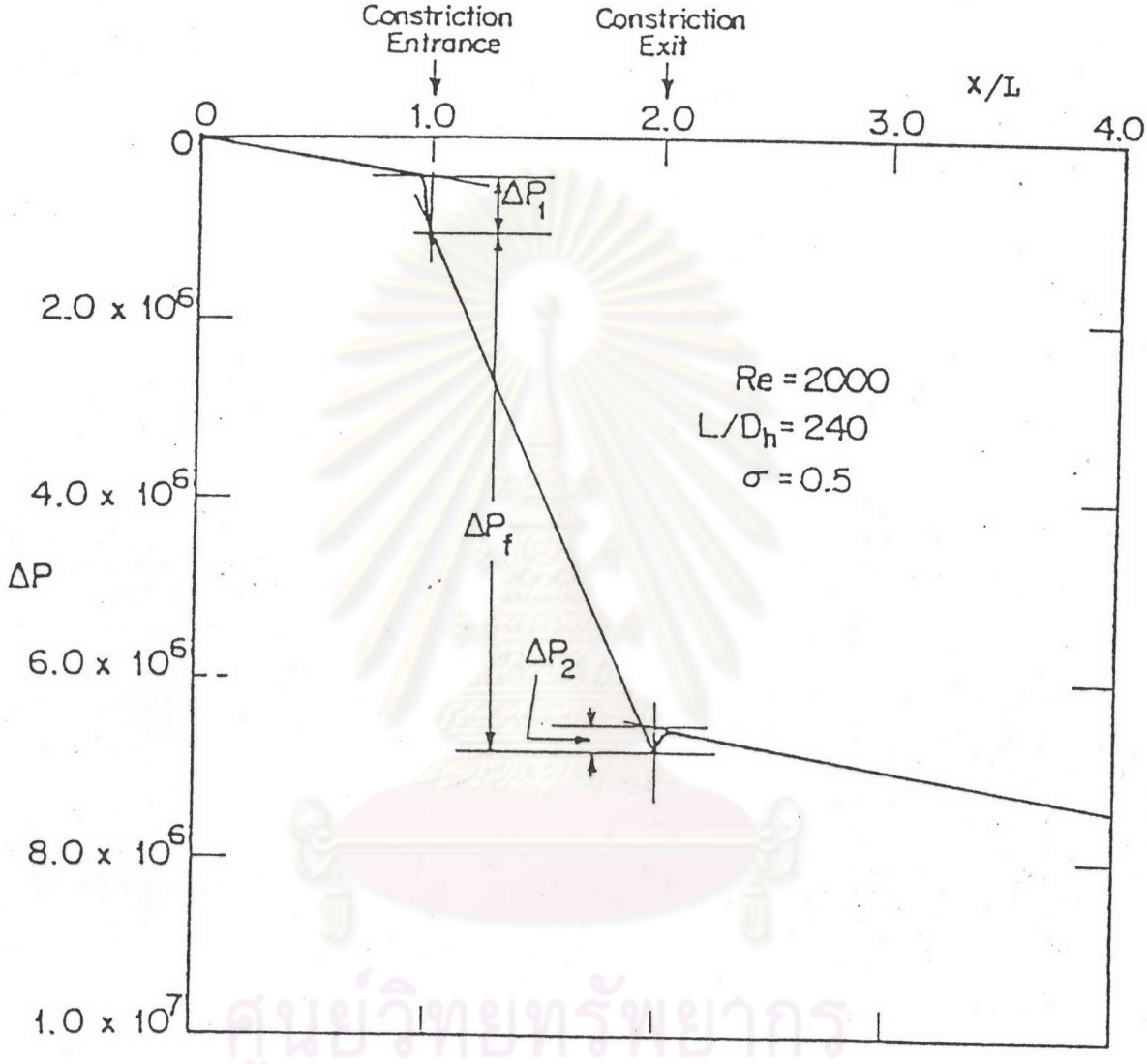

Fig.4.13a Pressure drop along mid-channel of long constricted parallel duct for Re = 2000, L/D_h = 240 and σ = 0.5. [3]

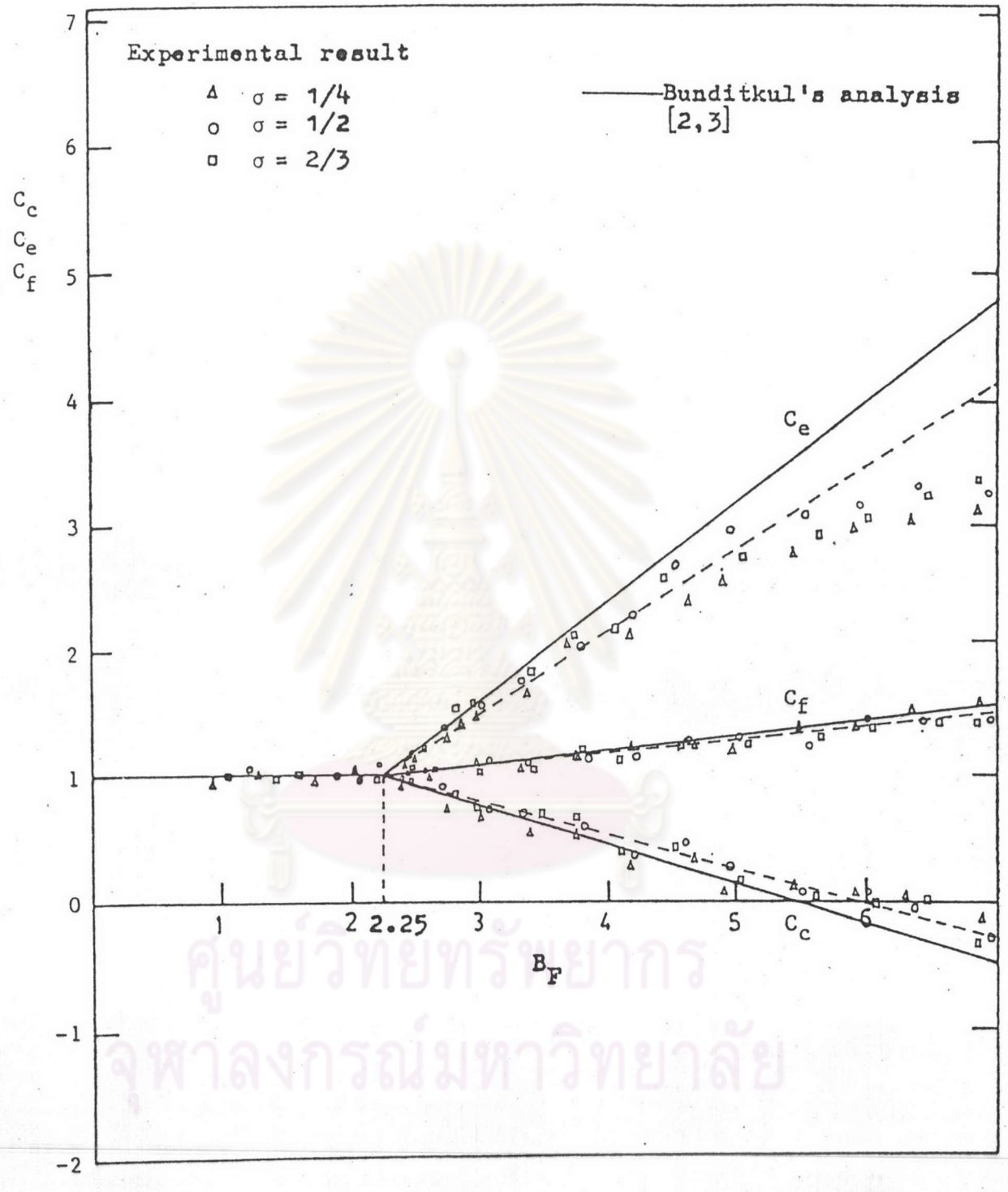

Fig. 4.14 Correction factor for loss coefficients and Fanning friction factor for flow through constricted parallel duct.

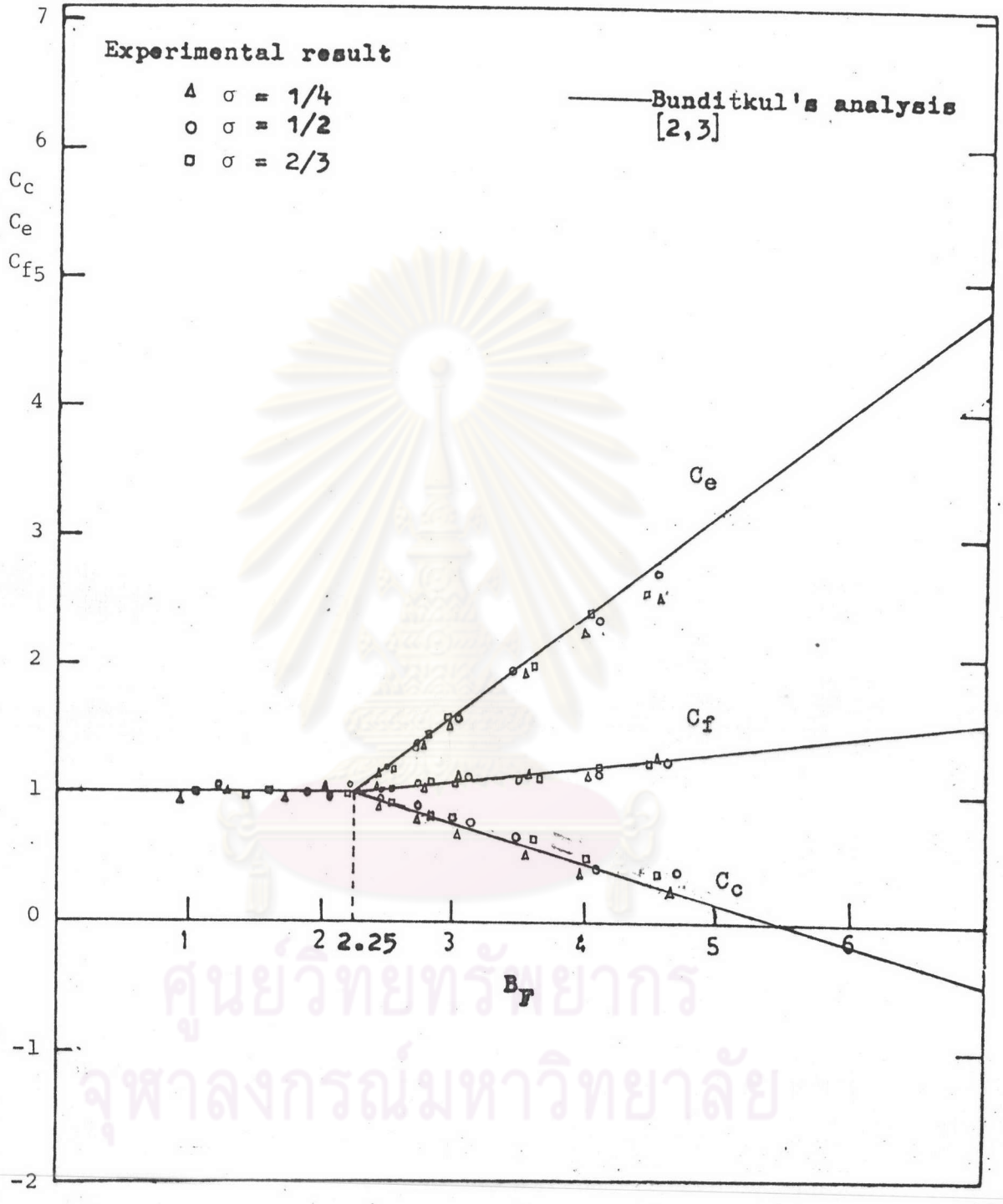

Fig. 4.14a Correction factors for loss coefficients and Fanning friction factor for flow through constricted parallel duct - with Re < 1600

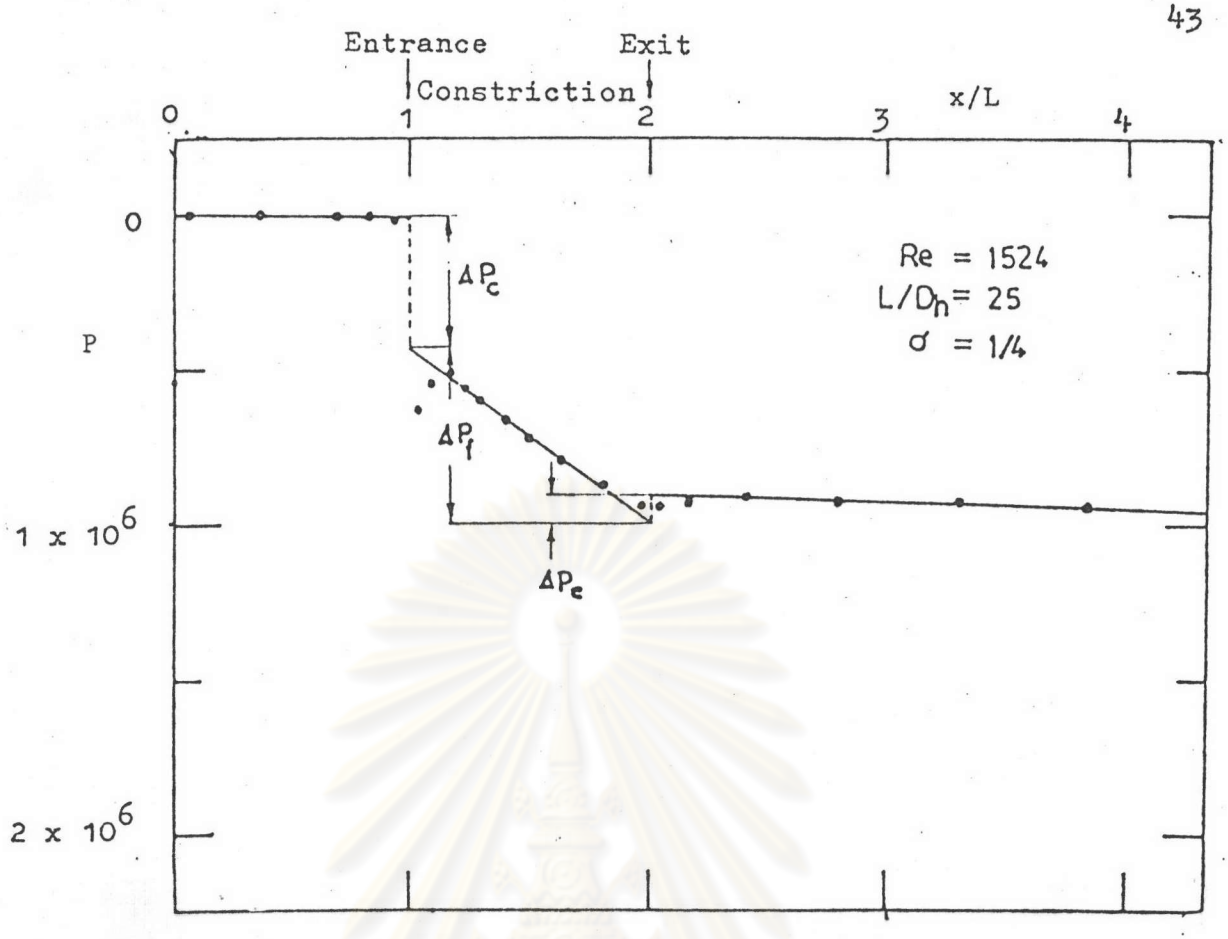

Fig. 4.15 Dimensionless axial pressure distribution for $\sigma = 1/4$, $L/D_h = 25$ and $Re = 1524$.

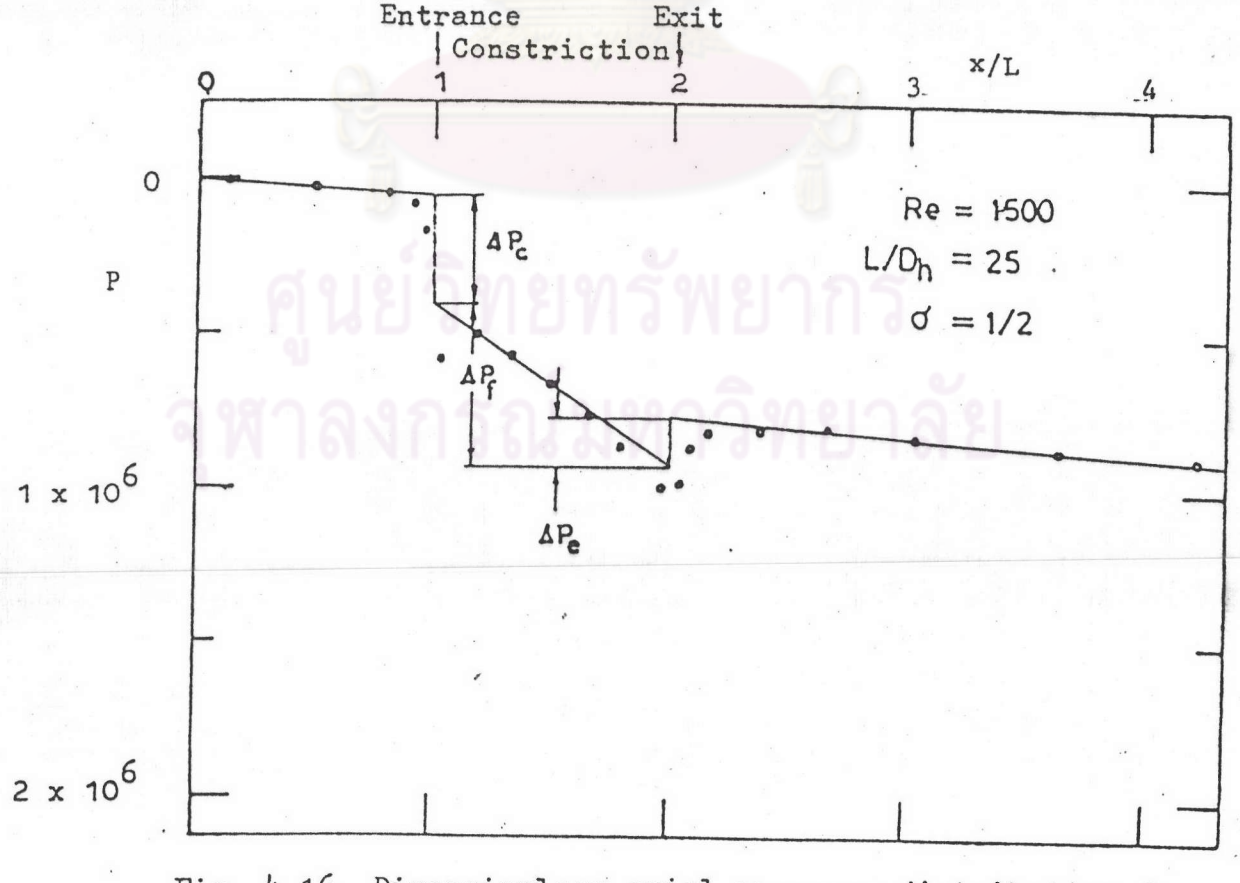

Fig. 4.16 Dimensionless axial pressure distribution for $\sigma = 1/2$, $L/D_h = 25$ and $Re = 1500$.

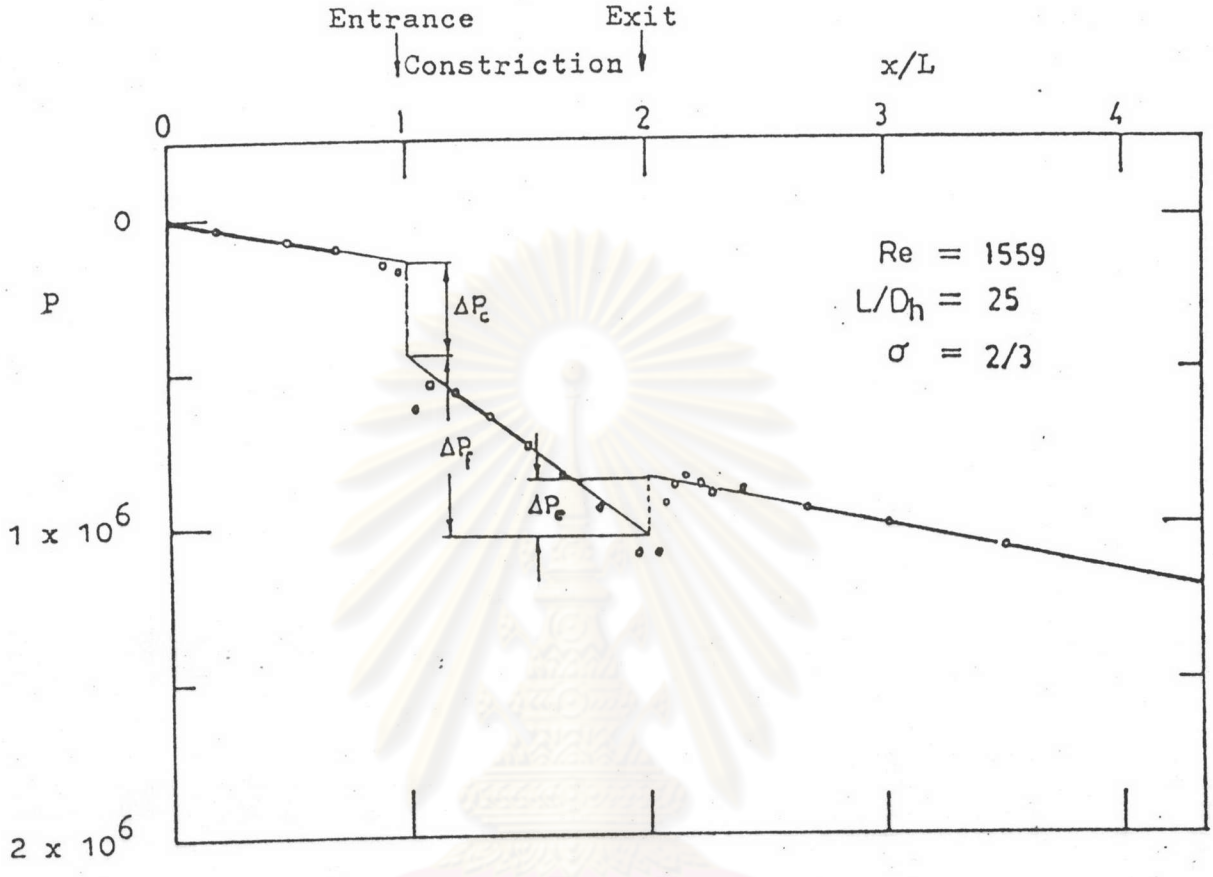

Fig. 4.17 Dimensionless axial pressure distribution for $\sigma = 2/3$, $L/D_h = 25$ and $Re = 1559$.

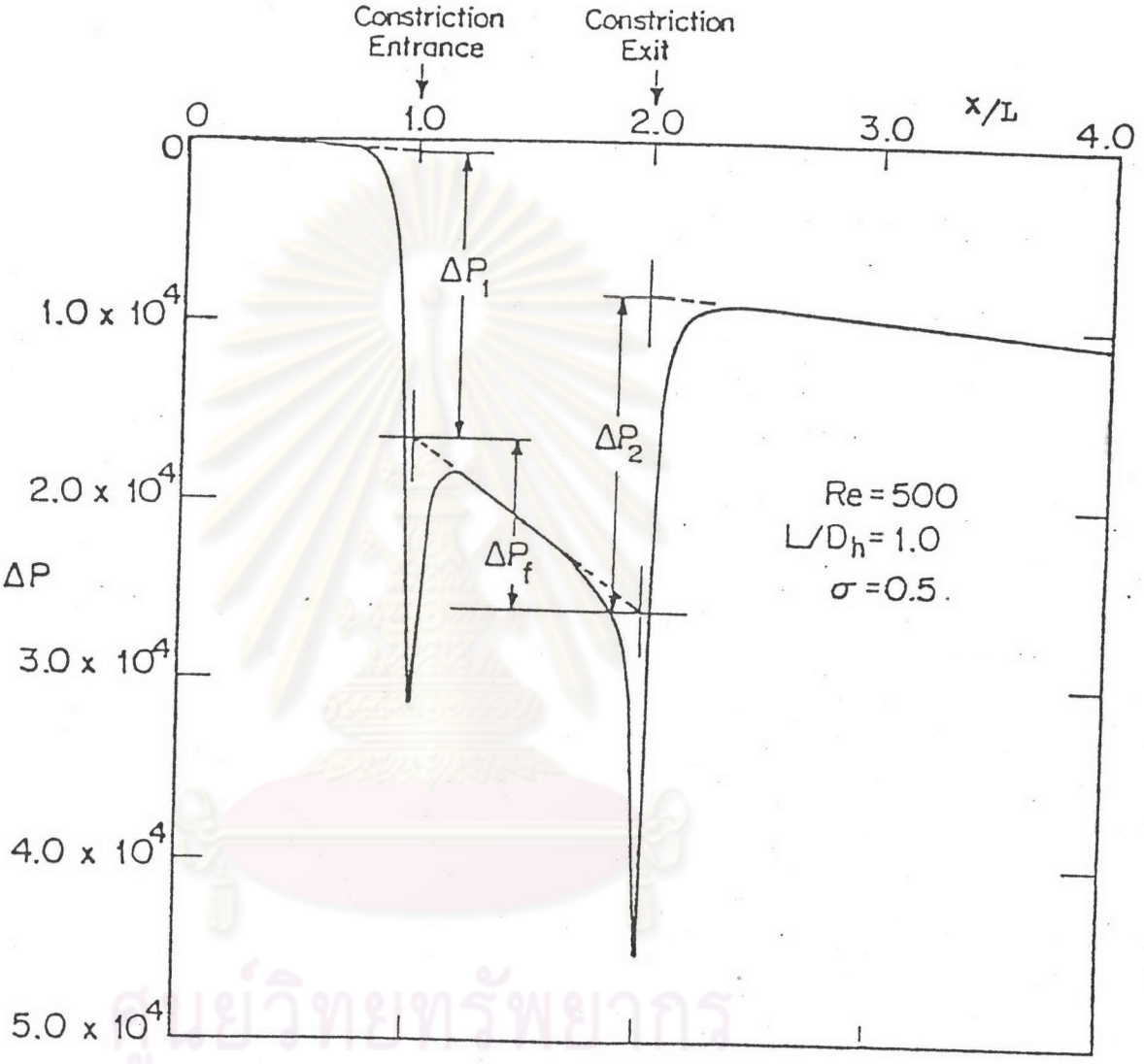

Fig.4.18 Pressure drop along mid-channel for Re = 500, L/D_h = 1 and σ = 0.5. by numerical analysis [3]